



# Dynamical Surface Imaging of $\lambda$ Andromedae

Arturo O. Martinez<sup>1,2</sup> , Fabien R. Baron<sup>1,2</sup> , John D. Monnier<sup>3</sup> , Rachael M. Roettenbacher<sup>4</sup> , and J. Robert Parks<sup>5</sup><sup>1</sup>Center for High Angular Resolution Astronomy, 25 Park Place NE #605, Atlanta, GA 30303-2911, USA; [aomartinez@chara.gsu.edu](mailto:aomartinez@chara.gsu.edu)<sup>2</sup>Department of Physics and Astronomy, Georgia State University, 25 Park Place NE #605, Atlanta, GA 30303-2911, USA<sup>3</sup>Department of Astronomy, University of Michigan, Ann Arbor, MI 48109-1090, USA<sup>4</sup>Yale Center for Astronomy and Astrophysics, Department of Physics, Yale University, New Haven, CT 06520-8120, USA<sup>5</sup>Department of Physics and Astronomy, George Mason University, 4400 University Drive Fairfax, VA 22030-4444, USA

Received 2020 November 18; revised 2021 May 27; accepted 2021 May 28; published 2021 July 27

## Abstract

We present temperature maps of RS CVn star  $\lambda$  Andromedae, reconstructed from interferometric data acquired in 2010 and 2011 by the Michigan Infra-Red Combiner instrument at the Center for High Angular Resolution Astronomy Array. To constrain the stellar parameters required for this imaging task, we first modeled the star using our GPU-accelerated code SIMulation and Modeling Tool for Optical Interferometry. The stellar surface was then imaged using our open source interferometric imaging code ROTational Image Reconstruction, in the process further refining the estimation of stellar parameters. We report that the measured angular diameter is  $2.742 \pm 0.010$  mas with a limb-darkening coefficient of  $0.231 \pm 0.024$ . While our images are consistent with those of prior works, we provide updated physical parameters for  $\lambda$  Andromedae ( $R_* = 7.78 \pm 0.05 R_\odot$ ,  $M_* = 1.24 \pm 0.72 M_\odot$ , and  $\log L/L_\odot = 1.46 \pm 0.04$ ).

*Unified Astronomy Thesaurus concepts:* [Astronomy data analysis \(1858\)](#); [Observational astronomy \(1145\)](#); [Late-type stars \(909\)](#); [Starspots \(1572\)](#); [Stellar rotation \(1629\)](#); [Interferometry \(808\)](#); [Long baseline interferometry \(932\)](#); [Optical interferometry \(1168\)](#)

## 1. Introduction

Observing stellar surfaces provides insight to the physics within stellar interiors. We know that stars ranging from pre-main sequence to giants exhibit magnetic spot activity on their surfaces (Strassmeier 2009). Since the advent of space missions, such as Convection, Rotation and planetary Transits (CoRoT; Baglin et al. 2006a; Baglin 2006b) and Kepler (Borucki et al. 2010; Koch et al. 2010), many more stars have been observed to exhibit magnetic activity (Frasca et al. 2011; Fröhlich et al. 2012; Roettenbacher et al. 2013, 2016a; Nielsen et al. 2019; Santos et al. 2019). These stellar features constitute major sources of uncertainty trying to calculate accurate stellar physical parameters (e.g.,  $T_{\text{eff}}$  and  $R_*$ ; Somers & Pinsonneault 2015). Starspots have other astrophysical significance tying them to accurately determining exoplanetary parameters. Any uncertainties found in the host star's physical parameters are amplified to any of their planetary parameters, as deriving exoplanetary parameters are dependent on the parent star.

RS Canum Venaticorum (RS CVn) variables are known to present large magnetic starspots (Hall 1976; Kóvári et al. 2015; Roettenbacher et al. 2016b, 2017). These variables are often found in a binary system and the pair often consists of an evolved giant primary with the secondary being a smaller main-sequence companion. Magnetic spots in these systems are often easier to observe because of their relative size to the star, thus making RS CVn variables ideal targets. There are three main techniques routinely employed to image these systems: light-curve inversion, Doppler imaging, and interferometric imaging.

Photometric monitoring of these systems provides straightforward evidence for stellar spots, as shown in many systems observed by the Kepler spacecraft (e.g., Frasca et al. 2011; Fröhlich et al. 2012; Roettenbacher et al. 2013, 2016a). The inverse problem of imaging the stellar surface from photometry is called light-curve inversion (Wild 1989; Roettenbacher et al. 2013). A main drawback of broadband light-curve inversion is

that photometry only provides relative information about the latitude of starspots (Harmon & Crews 2000) and relies on a prior knowledge of the stellar limb-darkening. Light-curve inversion from multiband photometry alleviates the latitude ambiguities, hence resulting in more accurate solutions (Harmon & Crews 2000).

Doppler imaging (Goncharov et al. 1977; Rice et al. 1981) is the class of inverse methods for imaging stellar surfaces from spectroscopic data. This technique uses perturbations of absorption features on a star to better estimate the spot's latitude and longitude. However, there are still uncertainties in determining spot location for stars near edge-on rotation. High-resolution spectra are needed in Doppler imaging to distinguish the features due to the starspots in the absorption lines and to be able to accurately detect their locations. High rotational velocities rotationally broaden absorption lines and are required to ensure that the spectroscopic impact of a spot moving across the surface is shorter than the spot's evolution timescale. Piskunov & Wehlau (1990) determined lower bounds enabling Doppler imaging to be from 6–15 km s<sup>-1</sup>, which corresponds to spectrograph resolving powers of at least 20,000–50,000.

Contrary to Doppler imaging or light-curve inversion, interferometry provides unambiguous evidence that a spot is being shown without any assumptions on latitude. Interferometric modeling allows the determination of angular parameters, such as the inclination or position angle of a spotted star. However, interferometric observations can only be managed on a limited number of targets (i.e., relatively bright targets) when compared to photometric and spectroscopic targets, and furthermore only targets of sufficient angular size can be resolved from Earth. It was only in 2007 that interferometric synthesis imaging became possible (Monnier et al. 2007) thanks to longer baselines and the combination of light from four (and now up to six) different telescopes.



The Center for High Angular Resolution Astronomy (CHARA) Array is an interferometric array with six 1 m telescopes, in a Y-shaped configuration, and the world’s longest operational baseline (at 330 m) in optical interferometry. CHARA data has been analyzed to provide detailed images of rapid rotators (Monnier et al. 2007; Zhao et al. 2009; Che et al. 2011), binary systems (Zhao et al. 2008; Kloppenborg et al. 2010; Baron et al. 2012; Kloppenborg et al. 2015), and nova eruptions (Schaefer et al. 2014). To date, three RS CVn variable stars have been imaged with CHARA:  $\lambda$  Andromedae (Parks et al. 2021),  $\zeta$  Andromedae (Roettenbacher et al. 2016b), and  $\sigma$  Geminorum (Roettenbacher et al. 2017).

$\lambda$  Andromedae (HD 222107; hereafter  $\lambda$  And) is a bright G8III-IV RS CVn variable ( $V=3.82$ ,  $H=1.40$ ) with spots, and is included in the third edition of the Catalog of Chromospherically Active Binary Stars (Eker et al. 2008). It is a single-lined spectroscopic binary system with a rotation period of 54.07 days for the primary (Henry et al. 1995) and has a companion in asynchronous rotation. Walker (1944) found a nearly circular orbit for the system with an eccentricity of  $e=0.084 \pm 0.014$  and an orbital period of  $20.5212 \pm 0.0003$  days. The most recent estimate of the effective temperature and mass for the primary star of  $\lambda$  And is 4800  $\pm$  100K and  $1.3^{+1.0}_{-0.6} M_{\odot}$  (Drake et al. 2011) with its companion most likely being a low-mass main-sequence star or a massive brown dwarf based on the mass ratio calculation of  $q = 0.12^{+0.07}_{-0.04}$  (Donati et al. 1995). Parks et al. (2021) was the first to do 2D snapshot interferometric imaging of  $\lambda$  And using data obtained with CHARA. Their study estimated the angular diameter for the primary of  $\lambda$  And to be  $2.759 \pm 0.050$  mas, corresponding to a physical radius of  $7.831^{+0.067}_{-0.065} R_{\odot}$  given the Hipparcos distance of  $26.41 \pm 0.15$  pc (van Leeuwen 2007).

In this paper, we describe the process we followed to obtain a temperature map of the surface of  $\lambda$  And. In Section 2, we present data acquisition and reduction. In Section 3, we describe how we used the interferometric modeling code SIMTOI to obtain initial guesses of stellar parameters. We introduce the ROTIR imaging code in Section 4, then its application to the imaging of  $\lambda$  And in Section 5. The imaging results are compared with previous works in Section 6. We go on to discuss prospects beyond solid-body rotation in Section 7 and the search for the companion of  $\lambda$  And in Section 8. Finally, we discuss our conclusions and future work in Section 9.

## 2. Observations

We reuse the 2010 and 2011 data from Parks et al. (2021), shown in Table 1 and calibrators in Table 2 used for each respective year, for our analysis. These data were obtained using the CHARA Array (ten Brummelaar et al. 2005) with the Michigan Infra-Red Combiner (MIRC; Monnier et al. 2004) in the  $H$  band with the median wavelength of  $1.65 \mu\text{m}$ . The observations were done in prism mode ( $R=50$ ), which contain eight spectral channels. The data taken in 2010 were taken with a combination of four out of six telescopes, which provide six visibilities, three independent bispectrum amplitudes (triple amplitudes), and three independent bispectrum phases (closure phases). The 2011 data set benefited from MIRC having been upgraded earlier that year, allowing for simultaneous use of all six telescopes. These upgrades provided data sets to acquire up

to 15 visibilities, 10 independent triple amplitudes, and 10 independent closure phases for each spectral channel.

### 2.1. Data Reduction

Parks et al. (2021) detail the reduction steps and error corrections but we will briefly note some of their steps here. The data were reduced using the official IDL pipeline for reducing MIRC data (Monnier et al. 2007). Each block of raw fringe data contained coadded frames, and were corrected for any instrumental effects by background subtraction in order to remove instrumental noise and foreground normalization to correct for any pixel-to-pixel variation. Raw square visibilities, closure phases, and triple amplitudes are output through the use of Fourier transforms and are photometrically calibrated. The data were corrected for the atmospheric coherence time and optical changes in the beam path with the use of calibrator stars that were taken either immediately before or after the target  $\lambda$  And.

In the 2010 data, one of the calibrators 37 And (HD 5448) was found to be a binary by Che et al. (2012) and had its orbit fully characterized by Roettenbacher et al. (2016b). Parks et al. (2021) formed a comparison of using 37 And as either a single star calibrator or as a binary calibrator. They found that these comparisons only incurred an error of 1.24% for the square visibilities, which is well below the multiplicative error correction, and a closure phase standard deviation of  $1.14^{\circ}$ . We execute a separate reduction and calibration for the 2010 data set using the official MIRC reduction pipeline in order to correct for the 37 And binary calibrator. We use the more recent calibrator diameter estimates, whose values differ from Parks et al. (2021), for this new reduction and calibration. The data uncertainties also go through a post-calibration process to account for known systematic errors of the MIRC instrument.

For the 2010 data we kept the same systematic errors as Parks et al. (accepted). These errors are different compared to the 2011 data set as the quality of the 2010 data are taken with a four telescope configuration and are of lower quality while the higher quality 2011 data are taken with a six telescope configuration. A 15% multiplicative error correction was used in association with the transfer function, a  $2 \times 10^{-4}$  additive error correction was used in association with bias at low amplitudes for the square visibilities, and a 20% multiplicative error correction and a  $1 \times 10^{-5}$  additive error correction was used for the triple amplitudes. The same  $1^{\circ}$  error floor was used for the closure phases as was used in Zhao et al. (2011). We present the square visibilities and closure phases for the 2010 data set in Figure 1.

We use the same calibrator diameter estimates listed in Parks et al. (2021) since the 2011 data set has been reduced and calibrated. Even though different angular sizes were used for the calibration of the 2010 and 2011 data set for 7 And and  $\sigma$  Cyg, the differences between the two angular sizes reported in Table 2 are small and within their respective  $1\sigma$  errors. Systematic errors were taken into account during calibration similar to that of Monnier et al. (2012). A 10% multiplicative error correction was used in association with the transfer function for the 2011 data and a  $2 \times 10^{-4}$  additive error correction was used for the square visibilities. A 15% multiplicative error correction was used and a  $1 \times 10^{-5}$  additive error correction was used for all the triple amplitude data. Lastly, the same  $1^{\circ}$  error floor was used for the closure

**Table 1**  
CHARA Array Observations

UT Date	Average MJD	Baselines	Number of $ V ^2$ points	Number of Closure Phases	Rotation Phase of Primary	Calibrators
2010 Aug 02	55410.4	S1-E1-W1-W2 S2-E2-W1-W2	167	88	0.0	7 And, 37 And
2010 Aug 03	55411.3	S1-E1-W1-W2 S2-E2-W1-W2	454	264	0.012	$\sigma$ Cyg, 7 And, 37 And
2010 Aug 10	55418.3	S1-E1-W1-W2 S2-E2-W1-W2	425	288	0.146	$\sigma$ Cyg, 7 And, 37 And
2010 Aug 11	55419.3	S1-E1-W1-W2	215	136	0.164	$\sigma$ Cyg, 7 And, 37 And
2010 Aug 18	55426.3	S1-E1-W1-W2 S2-E2-W1-W2	429	272	0.293	$\sigma$ Cyg, 7 And, 37 And
2010 Aug 19	55427.3	S1-E1-W1-W2	406	264	0.312	$\sigma$ Cyg, 7 And, 37 And
2010 Aug 24	55432.3	S1-E1-W1-W2 S2-E2-W1-W2	526	320	0.404	$\sigma$ Cyg, 7 And, 37 And
2010 Aug 25	55433.3	S2-E2-W1-W2	120	72	0.423	$\sigma$ Cyg, 7 And, 37 And
2010 Sep 02	55441.3	S1-E1-W1-W2 S2-E2-W1-W2	522	336	0.570	7 And, 37 And
2010 Sep 03	55442.3	S1-E1-W1-W2 S2-E2-W1-W2	588	352	0.589	7 And, 37 And
2010 Sep 10	55449.3	S2-E2-W1-W2	336	192	0.718	7 And, 37 And
2011 Sep 02	55806.5	W1-S2-S1-E1-E2-W2	360	432	0.310	$\sigma$ Cyg, 7 And, 22 And, HR 653
2011 Sep 06	55810.5	W1-S2-S1-E1-E2-W2	392	376	0.384	$\sigma$ Cyg, 7 And, 22 And, HR 653
2011 Sep 10	55814.5	W1-S2-S1-E1-E2-W2	360	432	0.458	7 And, 22 And
2011 Sep 14	55818.5	W1-S2-S1-E1-E2-W2	864	1104	0.532	7 And, 22 And, HR 653
2011 Sep 19	55823.5	W1-S2-S1-E1-E2-W2	808	1120	0.624	7 And, 22 And, HR 653
2011 Sep 24	55828.5	W1-S2-S1-E1-E2-W2	200	240	0.716	7 And, 22 And, HR 653, $\eta$ Aur

**Note.** Here, we list the UT date, the average modified Julian date of the night of observation, the baselines used in their corresponding configuration, the number of useful squared visibility points obtained for the night, the number of useful closure phase points obtained for the night, the rotation phase for the primary star in  $\lambda$  And, and the calibrator stars that were used for each corresponding night. The rotation phase is derived by using the first observation in 2010 as the zero-point.

**Table 2**  
Calibrators for  $\lambda$  Andromedae

Calibrator Name	Calibrator Size (mas)	Source	Epoch Used
7 And (HD 219080)	$0.65 \pm 0.03$	Mourard et al. (2015)	2010
37 And (HD 5448)	$46.66 \pm 0.06$	Roettenbacher et al. (2016b) <sup>a</sup>	2010
$\sigma$ Cyg (HD 202850)	$0.542 \pm 0.021$	Zhao et al. (2008)	2010
7 And (HD 219080)	$0.676 \pm 0.047$	SearchCal (Bonneau et al. 2006)	2011
$\sigma$ Cyg (HD 202850)	$0.54 \pm 0.02$	Barnes et al. (1978)	2011
22 And (HD 571)	$0.591 \pm 0.041$	SearchCal (Bonneau et al. 2006)	2011
HR 653 (HD 13818)	$0.646 \pm 0.045$	SearchCal (Bonneau et al. 2006)	2011
$\eta$ Aur (HD 32630)	$0.336 \pm 0.023$	SearchCal (Bonneau et al. 2006)	2011

**Notes.** The angular sizes for the 2011 epochs are based on what was reported from Parks et al. (2021) since we use their reduced and calibrated data. We use updated angular sizes for each calibrator star in the 2010 epoch since we do a new and separate reduction and calibration. The differences in angular sizes for 7 And and  $\sigma$  Cyg used between the two years are small and within their  $1\sigma$  errors.

<sup>a</sup> This is the semimajor axis angular separation of the binary calculated by Roettenbacher et al. (2016b).

phases just as it was presented in Zhao et al. (2011). We present the square visibilities and closure phases for all of the 2011 data set in Figure 2.

### 3. Modeling $\lambda$ And with SIMTOI

The SIMulation and Modeling Tool for Optical Inteferometry (SIMTOI) is an interferometric modeling code<sup>6</sup> (Kloppenborg & Baron 2012a, 2012b; Kloppenborg et al. 2015) that uses a Graphical Processor Unit (GPU) to represent

stars and their environments in a three-dimensional framework. In SIMTOI, the stellar intensity maps are two-dimensional textures applied on top of orbiting/rotating three-dimensional stars. Once the scene is rendered, the GPU also powers the fast computation of interferometric observables. SIMTOI offers a large choice of global and local optimizers to solve Maximum A Posteriori (MAP) or model selection problems. Our first goal in using SIMTOI was to derive initial guesses for  $\lambda$  And's stellar parameters (such as its rotation axis), since our imaging code would be too slow to wade through the entire parameter space. Our second goal was to assess the potential number of spots present on the star via model selection. Both tasks were

<sup>6</sup> <https://github.com/bkloppenborg/simtoi>

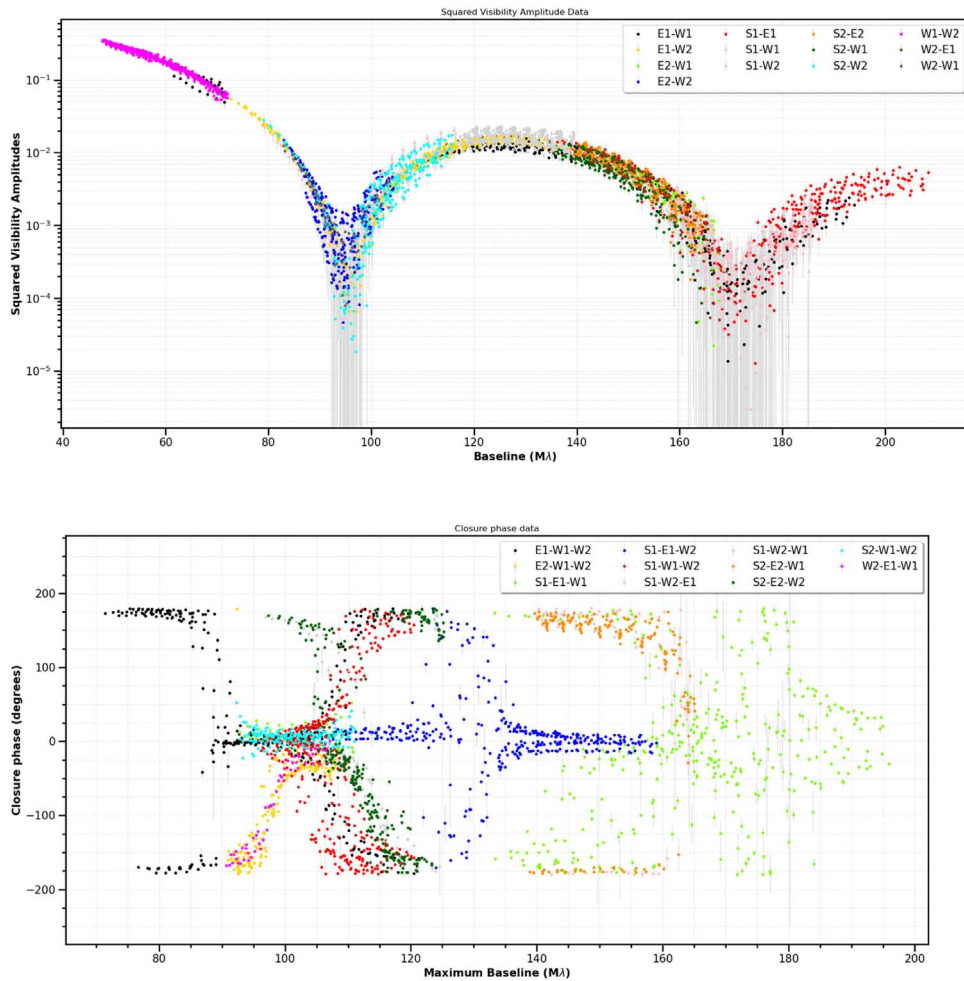


**Figure 1.** Top:  $|V|^2$  points are plotted against the baseline length (in  $M\lambda$ ) for a given baseline pair for all the data of  $\lambda$  And from the 2010 epoch. Bottom: Closure phase points are plotted against the baseline length (in  $M\lambda$ ) for the given baseline trio for the same 2010 data.

solved using the MultiNest optimizer (Feroz & Hobson 2008; Feroz et al. 2009, 2013), which implements the Importance Nested Sampling algorithm.

### 3.1. Modeling $\lambda$ And

We devised models of  $\lambda$  And with different number of circular spots, from three to six. Six parameters were used to model the star itself: rotation period, rotation axis (inclination and position angles), temperature, angular diameter, and coefficient of the power limb-darkening law (Hestroffer 1997). The stellar parameters were given uniform prior distributions within a wide range of values, based on the stellar parameters listed in Parks et al. (2021) as a starting point (e.g.,  $\pm 20^\circ$  for angular parameters). Four parameters were used per spot: longitude, latitude, diameter, and flux. These spot parameters were also given uniform distribution. In particular, their location was not constrained.

For each data set—2010 or 2011—SIMTOI renders an image per epoch (day). The rendering resolution was set to a  $64 \times 64$  image with a  $0.05 \text{ mas pixel}^{-1}$  resolution. MultiNest was run for each model and converged after a few hours, providing MAP parameter values, as well as the marginal likelihood values (the so-called  $\log Z$ ).

### 3.2. Modeling Results

We report the  $\chi^2$  and  $\log Z$  values for each spot model in Table 3. We also provide the approximate nominal values for the physical parameters. MultiNest does provide error bars, but since they do not account for systematic errors, they are vastly underestimated. While one could bootstrap the data before MultiNest runs, this would be too computationally intensive and yet still imprecise due to our approximate modeling of spots. Our model spots are circular, which may be an unrealistic assumption, but is sufficient to identify the main potential location of intensity peaks on the surface. The  $\log Z$  values are maximal for the five spot model for the 2010 data, and the four-spot model for the 2011 data. The corresponding reduced  $\chi^2$  values are low for the 2011 data and much higher for 2010. Setting aside the possible differences in error calibration between 2010 and 2011, this would indicate that the 2010 surface map is much more complex than the 2011 one (which we did confirm during imaging).

We ultimately choose the four-spot model for the 2011 data as the best representative model that produces the most accurate parameterization of  $\lambda$  And. The estimated 54.2 day rotation period of the primary from our model using the 2011 data set is consistent with other works. Henry et al. (1995) reports a rotation period 54.07 days from their photometric analysis while Parks et al. (2021) reports a

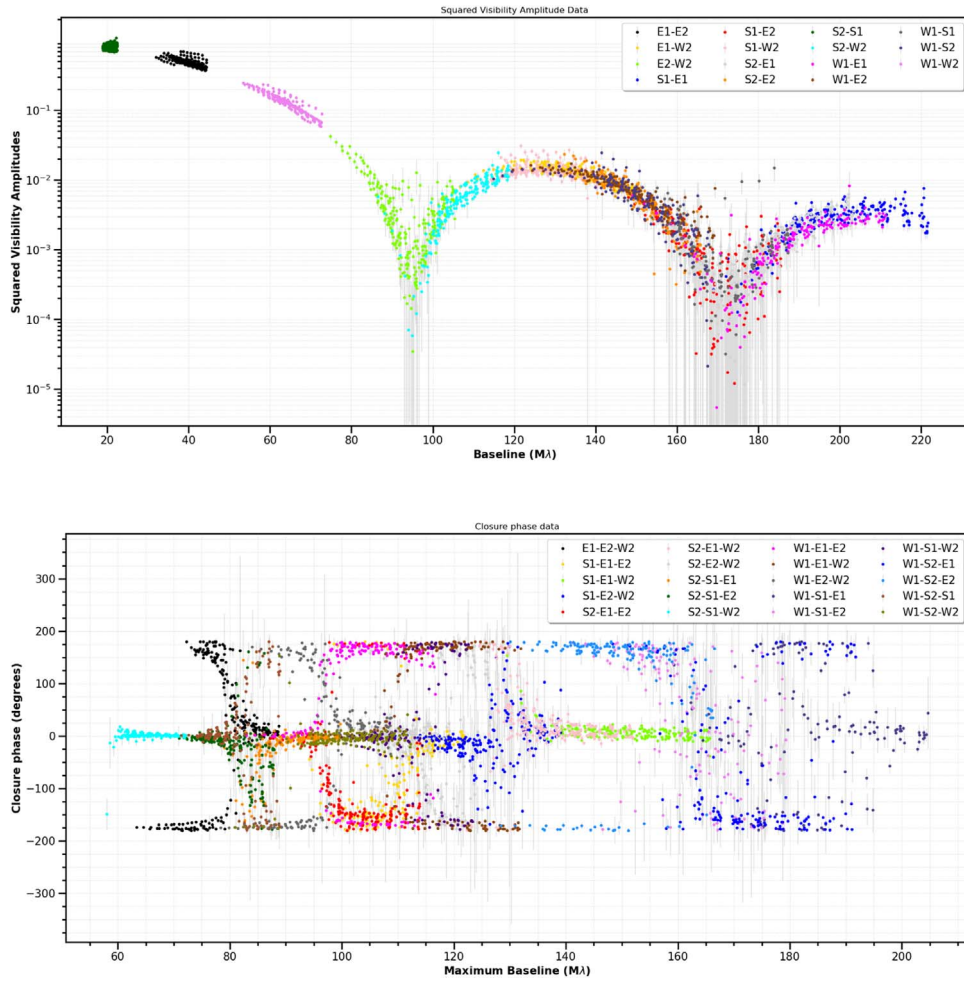


**Figure 2.** Top:  $|V|^2$  points are plotted against the baseline length (in MA) for a given baseline pair for all the data of  $\lambda$  And from the 2011 epoch. Bottom: Closure phase points are plotted against the baseline length (in MA) for the given baseline trio for the same 2011 data.

**Table 3**  
SIMTOI Model Results

Number of Spots	Importance Nested		$\chi^2_\nu$	
	Sampling Value (ln Z)		2010 Data	2011 Data
3	-67599.448761	10433.734767	56.855263	8.020829
4	-5968.401012	36157.820383	17.114268	3.102330
5	1420.128960	32785.721919	11.372939	3.710609
6	-45295.096429	30193.016672	38.679240	4.211333
Physical parameters (four-spot model based on 2011 data)	Value			
$R_*$ (mas)	1.37			
Limb-darkening coefficient	0.22			
Inclination (deg)	86.4			
Position angle (deg)	26.7			
Rotation period (days)	54.2			

**Note.** Higher ln Z value is better, lower  $\chi^2_\nu$  is better. No error bars are calculated since the models from SIMTOI using Multinest does not currently generate reliable error bars. We rely on the imaging results for more precise measurements and calculation of errors.

54.02 ± 0.88 day rotation period from their own photometric analysis and an average of a 56.9 ± 8.8 day rotation period from their interferometric analysis. While the 2010 data set had

a larger rotation phase coverage than the 2011 data set, the rotation period based on the 2011 data are overall more reliable based on MultiNest results and the fitting of the model to the

data. This is most likely due to the larger amount of  $(u, v)$  coverage, number  $(u, v)$  points, triple amplitudes, and closure phase points in the 2011 data set compared to the 2010 data set. This calculated period from the four-spot model using the 2011 data is consistent with previous works.

#### 4. ROTIR

Our code ROTational Image Reconstruction<sup>7</sup> (ROTIR) is an open source Julia code (Baron & Martinez 2018, 2021) which models the stellar surface temperatures of single stars or binary systems as two-dimensional arrays on top of a stellar geometry. The stellar geometry itself is defined either by analytic formulas (ellipsoids, fast rotators) or by solving Roche equations. In imaging and model-fitting problems, ROTIR makes use of the optimization packages *OptimPack* (Thiebaud 2002) and *NLOpt* (Johnson 2008) to maximize the posterior probability of the model.

##### 4.1. Geometry Setup

ROTIR relies on the package *OITTOOLS*<sup>8</sup> (Baron et al. 2019) to read in our data, split up or combine our data temporally, and plot any images featured in this work.

Once the interferometric data are read, we define the stellar parameters and orientation of our object. Our code requires several parameters: the angular size at the pole in milliarcseconds, the surface temperature, the fraction of the critical angular velocity if the star is rapidly rotating, the limb-darkening law and its corresponding coefficient(s), the exponent needed if there is any gravity darkening (von Zeipel 1924), the difference in angular velocity between the equator and the pole, the inclination, position angle, and rotation period of the star. Our code allows the user to choose between three different limb-darkening laws: a quadratic law, logarithmic law, or Hestroffer law (commonly known as the power law; Hestroffer 1997).

Our geometrical setup starts with selecting a tessellation scheme. Two schemes have been implemented so far: the HEALPix tessellation (Górski et al. 2005) and the latitude/longitudinal scheme. HEALPix presents the advantage of equal area tessels, provided the star does not depart too much from a spherical shape. The latitude/longitudinal scheme allows for simulating differential rotation, but requires more tessels to represent the surface. As part of this work we tested both tessellation schemes, which result in qualitatively identical maps. Most results presented in this paper were obtained with the latitude/longitude scheme. The number of pixels per angular diameter was chosen based on the estimated angular diameter size divided by the imaging resolution limit. Therefore, the minimum total number of pixels required across the surface of a star would simply be the number of latitude pixels times the number longitude pixels.

For the latitude/longitude scheme, the number of latitude pixels is based on the number of pixels per angular diameter since the latitude range spans from  $-90^\circ$  to  $90^\circ$  and the number of longitude pixels is twice the number of pixels per angular diameter since the longitude ranges from  $0^\circ$ – $360^\circ$ . We number the vertices of the polygon by 1, 2, 3, 4 in a counterclockwise direction when viewed along the direction of the normal. A

fifth element is also included for each pixel and defined to be at the center of each pixel.

Once the user has chosen a tessellation scheme and calculated the number of pixels required for imaging, the user then has the choice of choosing between three different geometries: a scaled unit sphere, an oblate spheroid, or a Roche object.<sup>9</sup> The order in which the pixels are mapped out on the surface of the star are counterclockwise when viewed along normal of the positive  $z$  direction on the  $(x, y, z)$  plane.

The surface area  $A_n$  is calculated for all  $n$  pixels in order to determine the amount of relative flux coming from the star with the following:

$$A_n = \frac{1}{2} \sum_{j=1}^m (\mathbf{v}_j \wedge \mathbf{v}_{j+1}) \cdot \hat{\mathbf{z}}, \quad (1)$$

where  $\mathbf{v}$  is the vector of  $(x, y)$  projected positions of the  $n$ th pixel in a two-dimensional  $(x, y)$  plane at the  $j$ th corner with  $m$  number of corners in the polygon of choice,  $\cdot$  is the scalar product, and  $\wedge$  the vector cross product operator. The  $m+1$  corner here points back to the first corner of the pixel.

Once the surface area of each pixel is calculated with the desired limb-darkening law, the Fourier transform  $S$  is done on every pixel for a three-dimensional object (Lee & Mittra 1983; Chu & Huang 1989; McInturff & Simon 1991) in order to compare the frequencies of our data on the  $(u, v)$  plane by using the following equation:

$$S(\mathbf{k}) = \sum_{j=1}^m \hat{\mathbf{z}} \cdot [(\mathbf{v}_{j+1} - \mathbf{v}_j) \wedge \mathbf{k}] \frac{\text{sinc}[\mathbf{k} \cdot (\mathbf{v}_{j+1} + \mathbf{v}_j)]}{i2\pi|\mathbf{k}|^2} \times \exp[-i\pi\mathbf{k} \cdot (\mathbf{v}_{j+1} + \mathbf{v}_j)], \quad (2)$$

where  $\mathbf{k}$  is a vector containing each  $u$  and  $v$  frequency on the  $(u, v)$  Fourier plane. We use the flux to visibility matrix  $S$  to compute the model visibilities using

$$\mathbf{V} = \frac{S(\mathbf{L} \circ \mathbf{T})}{\mathbf{A}^\top (\mathbf{L} \circ \mathbf{T})}, \quad (3)$$

where  $\mathbf{V}$  is the model complex visibility vector,  $\mathbf{T}$  is the temperature map vector,  $\mathbf{L}$  is the limb-darkening map,  $\circ$  is the Hadamard (element by element) vector product, and the division is the Hadamard division.

##### 4.2. Differential Rotation Option

The user can select whether or not to turn on the option to simulate differential rotation. The equation for differential rotation (Henry et al. 1995) used in our code is in the form

$$\Omega(\Psi) = \Omega_{\text{eq}} - \Delta\Omega \sin^2 \Psi, \quad (4)$$

where  $\Psi$  is the latitude,  $\Omega(\Psi)$  is the rotation rate at a specific latitude,  $\Omega_{\text{eq}}$  is the rotation rate at the equator, and  $\Delta\Omega$  is the difference in angular velocity between the equator and the pole. This difference between angular velocity in the equator and the pole is related to the differential rotation coefficient,  $k$ , or the surface shear parameter,  $\alpha$ , commonly found in the literature (e.g., Henry et al. 1995; Davenport et al. 2015; Kóvári et al. 2015) and

<sup>7</sup> <https://github.com/fabienbaron/ROTIR.jl>

<sup>8</sup> <https://github.com/fabienbaron/OITTOOLS.jl>

<sup>9</sup> Technically, the model of the star is a polyhedron since the surface is made up of many different pixels and not one solid surface. In order to describe the overall shape of the star, we choose to name them as 3D objects instead of polyhedrons.

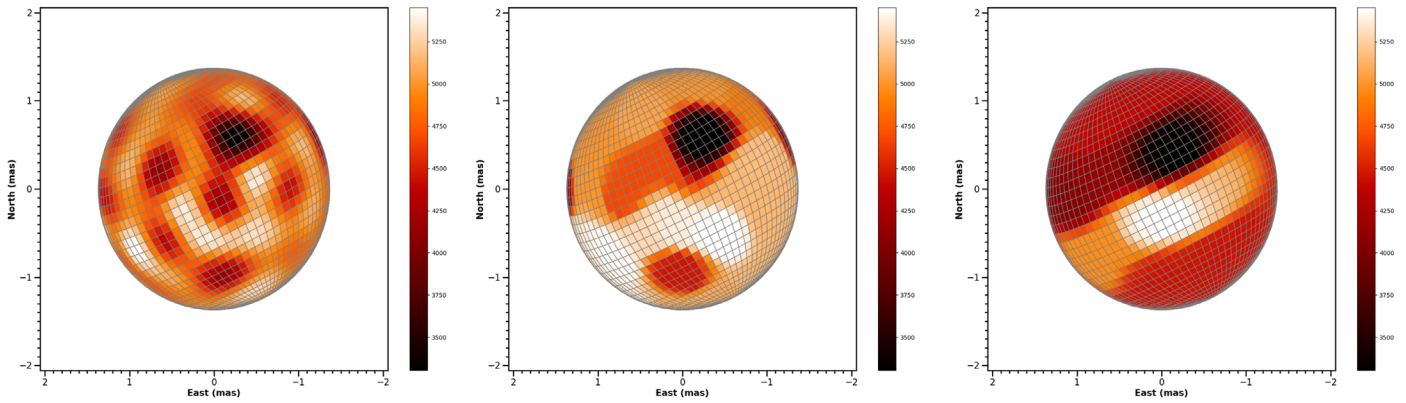


**Figure 3.** Left: Here, we show an example of a reconstruction made with a very weak hyperparameter ( $\mu = 0.0001$ ). This is close to the classic example of overfitting an image based on the data. Middle: Here, we show where there is a good balance of fitting the data to a model and the use of a hyperparameter ( $\mu = 0.01$ ). Right: Here we show an example where the hyperparameter is dominant ( $\mu = 0.5$ ) and very loosely based on the data fitting the model. All three temperature maps are in Kelvin.

is defined through the following equation:

$$k = \frac{\Omega_{\text{eq}} - \Omega_{\text{pole}}}{\Omega_{\text{eq}}}, \quad (5)$$

or in terms of the polar and equatorial rotational periods as

$$k = \frac{P_{\text{pole}} - P_{\text{eq}}}{P_{\text{pole}}}. \quad (6)$$

#### 4.3. First Use of Regularization

Fitting a model to the data with no prior constraints will produce unrealistic images due to overfitting. The *Maximum A Posteriori* method balances the likelihood term with our prior expectations of what the temperature map should look like. The optimal temperature map  $x_{\text{opt}}$  is then found as

$$x_{\text{opt}} = \operatorname{argmin}_{x \in \mathbb{R}^n} \{ \chi^2(x) + \mu R(x) \}, \quad (7)$$

where  $\chi^2(x)$  is the chi square fit of the data to the model,  $R(x)$  is the regularization, and  $\mu$  is the hyperparameter setting the relative weight of the regularizer versus the likelihood.

We implemented three different regularizations for use in ROTIR: positivity,  $l_2$  norm, and total variation. Positivity enforces a non-negative temperature map. The  $l_2$  norm takes the square root of the sum of square values for each pixel and penalizes pixel values straying too far from the average value. Our third regularizer is total variation which computes the spatial gradient of the model image and penalizes large temperature fluctuations between neighboring pixels such that it shows smoother transitions on a local scale.

## 5. Applying ROTIR to $\lambda$ And

For  $\lambda$  And, we use positivity and total variation as the two regularizers necessary to determine the best image. Using the  $l$ -curve method (Renard et al. 2011), we choose a weight of  $\mu = 0.01$  that has a small amount of regularization before entering into a regularization dominated regime. We show examples of strong and weak regularization in Figure 3 for data of  $\lambda$  And taken on 2011 Sep 14 to prove why we need a good balance between regularization and pure model fitting when finding an optimum image.

In order to determine of the number of tessels required on the surface of the star, we use the parameters we obtained from

modeling  $\lambda$  And using SIMTOI. Knowing that the CHARA angular resolution limit is  $\theta \approx 0.60$  mas at the  $H$  band ( $\lambda = 1.61$   $\mu\text{m}$ ), we estimate that we need 40 pixels across the visible equator to meet Nyquist sampling (imaging resolution limit is  $\theta \approx 0.30$  mas in the  $H$  band). Therefore, we use 80 pixels around each latitude, including pixels behind the star, and 40 pixels across each longitude for a total of 3200 pixels on the surface of the star. Our sampling of pixels across the resulting images are solely based on the number of pixels on the surface of the star and not the overall field as the field size can be arbitrarily chosen based on the plotting axes.

#### 5.1. A First Look at Imaging

In order to find the best geometrical setup for primary star in  $\lambda$  And, we test both a spherical star and a Roche lobe shape to see if there is any signs of major Roche lobe overflow. While Donati et al. (1995) and Parks et al. (2021) both suggest that there is no Roche lobe overflow, we decide to investigate this for  $\lambda$  And since slight oblateness was found in another RS CVn variable,  $\zeta$  Andromedae (Roettenbacher et al. 2016b).

We start with the parameters from SIMTOI to create our spherical star and, with the addition of the longitude of the ascending node, argument of periapsis, and eccentricity found in Walker (1944), create our Roche lobe geometry. Donati et al. (1995) states that  $\lambda$  And is coplanar, therefore we use the inclination rotation axis of the primary star as the inclination of the orbit. We use the same hyperparameter and apply a uniform temperature map across the whole star as an initial condition for both geometries. Using a Julia package called *OptimPack*<sup>10</sup> that solves for an optimum temperature map through a quasi-Newtonian method (Thiebaud 2002), we obtain for the best temperature map given our all our data in a given year. This algorithm compares the Fourier transforms from Section 4.1 to the 2011 data to solve for the best temperature map.

The resulting criterion for the Roche lobe geometry is higher ( $\chi^2(x) + \mu R(x) = 6288$ ) when directly comparing it to a spherical geometry (criterion = 4489). We also find that the pole-to-equator ratio at the L1 Lagrangian point for the primary is 0.9967. With these two calculations, we determine that a spherical geometrical shape for the primary of  $\lambda$  And is an acceptable approximation for the true shape of the star.

<sup>10</sup> <https://github.com/emmt/OptimPackNextGen.jl>

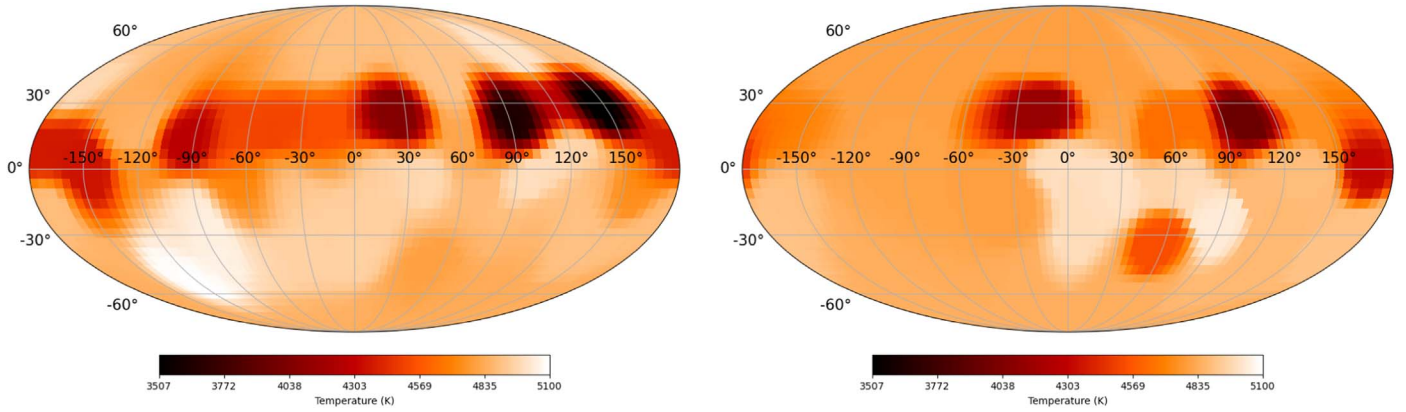


**Figure 4.** Here, we show a Mollweide plot of  $\lambda$  Andromedae for the 2010 epoch (left) and 2011 epoch (right) using our ROTIR code. We combine our 11 nights of data in 2010 across 39 nights and 6 nights of data in 2011 across 22 nights to make the temperature map for the 2010 epoch and 2011 epoch, respectively. Both plots use the first date of the 2010 data as the zero-point rotation phase and are shifted accordingly. We note that the pixels not within the observing line of sight are calculated by starting at the effective temperature from Drake et al. (2011) and modified through *OptimPack*. Areas where the  $\lambda$  And is not observed (i.e., latitudes below  $-85^\circ$  for both epochs and longitudes between  $-124^\circ$  and  $-90^\circ$  for the 2011 epoch) have temperatures near the input effective temperature of 4800 K.

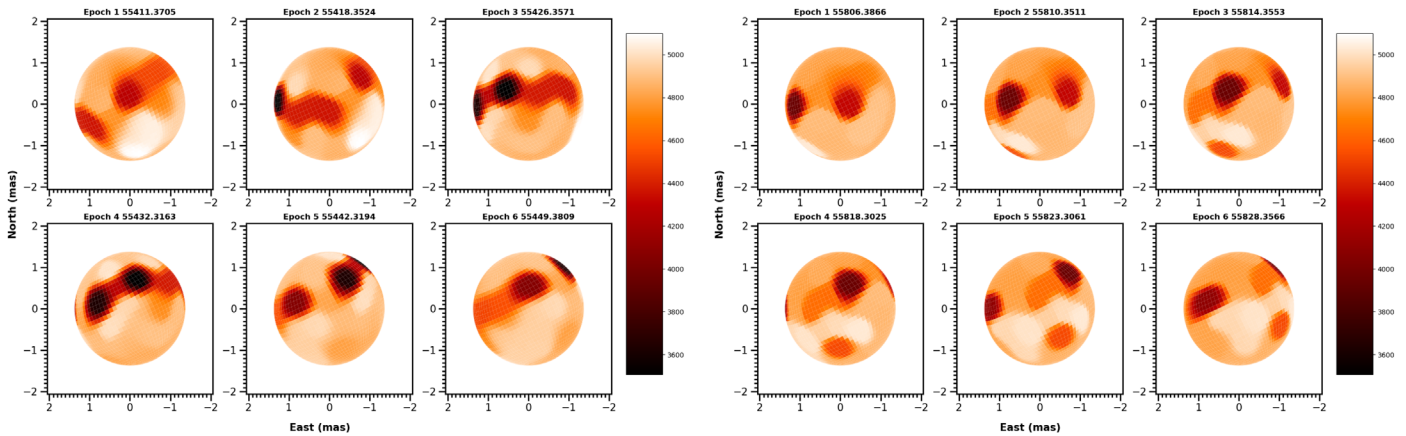


**Figure 5.** We show temperature maps (in Kelvin) of  $\lambda$  Andromedae for the 2010 epoch (left) and 2011 epoch (right) using our ROTIR code. Here, we note that our 2010 temperature map panels do not reflect all 11 nights of data but only show a subset of 6 nights. The nights for the 2010 temperature map panels are chosen by only selecting one of two consecutive observational nights and having the next temperature map panel be separated by at least 6 nights (i.e., 2010 Aug 03, 2010 Aug 10, 2010 Aug 18, 2010 Aug 24, 2010 Sep 03, and 2010 Sep 10).

Once we have determined that the spherical geometrical setup is the most optimal for  $\lambda$  And and choose the most optimal regularization weight, we are now set for calculating the best fit for the temperature map. We present the resulting Mollweide maps of  $\lambda$  And for both epochs in Figure 4. These maps reflect no time variability and assume that  $\lambda$  And is undergoing solid-body rotation. A better representation of the temperature maps are shown in Figure 5 for each given night in 2010 and 2011.

A first look at the temperature maps between the 2010 and 2011 epochs shows a few interesting characteristics about  $\lambda$  And's surface. Comparing the two temperature maps show notable similarities for two spots in the northern hemisphere between the two epochs (i.e., the spot around  $20^\circ$  latitude and  $\sim 100^\circ$  longitude, and the spot around  $0^\circ$  latitude and  $170^\circ$  in both epochs). There are two other notable spots that either disappear or appear from one epoch to the next. The spot in the 2010 epoch around  $30^\circ$  latitude and  $150^\circ$  longitude seems to have disappeared within the 2011 epoch. A spot seems to be forming within the 2011 map in the southern hemisphere around  $-40^\circ$  latitude and  $50^\circ$  longitude with hints of its emergence with similar place in the 2010 epoch. We note that

the spot in the 2010 epoch around  $15^\circ$  latitude and  $-90^\circ$  does not appear in the 2011 epoch. This is most likely due to missing rotational phase coverage in the 2011 data set.

## 5.2. Refinement of Physical Parameters

After finding the best model from SIMTOI, we use the parameters from the four-spot model based on the 2011 data and use the bootstrap method. We apply the bootstrap method in order to find the final parameters and errors for the primary component of  $\lambda$  And. We use 50 bootstrap iterations to solve for only four parameters: angular radius, the limb-darkening coefficient, inclination, and position angle. We choose to leave the rotation period of the primary fixed throughout this bootstrap because there is a degeneracy toward lower rotation periods. We believe that this is due to the fitting algorithm in ROTIR choosing the difference between the first and last observing date (in a given epoch) for the period instead of the true rotational period. Our bootstrap is dependent on the NLOpt package (Johnson 2008) and Nelder–Mead simplex method (Box 1965; Nelder & Mead 1965; Richardson & Kuester 1973) within NLOpt for obtaining our final parameters with their corresponding errors. We restrict lower and upper bounds



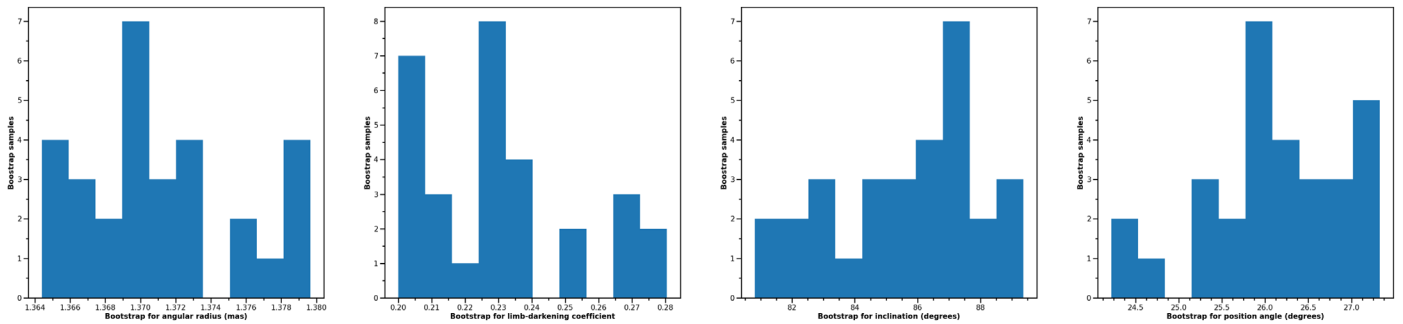


**Figure 6.** Here, we show the results of using the bootstrap method varying angular radius, the limb-darkening coefficient, inclination, and position angle. We use 50 bootstraps in order to calculate the final parameters of  $\lambda$  Andromedae and bin them into 10 different bins. The x-axis here shows the range of the parameters from all the bootstraps and the y-axis show the number of bootstraps within each bin. While we plot calculated values for each bootstrap, we note that the full range for each parameter are the following: [1.35, 1.39] for angular radius, [0.2, 0.3] for the limb-darkening coefficient, [70.0, 90.0] for inclination, and [20.0, 30.0] for position angle. The final parameters are calculated from taking the average of each respective parameter with their associated errors calculated from the standard deviation of the bootstrap results.

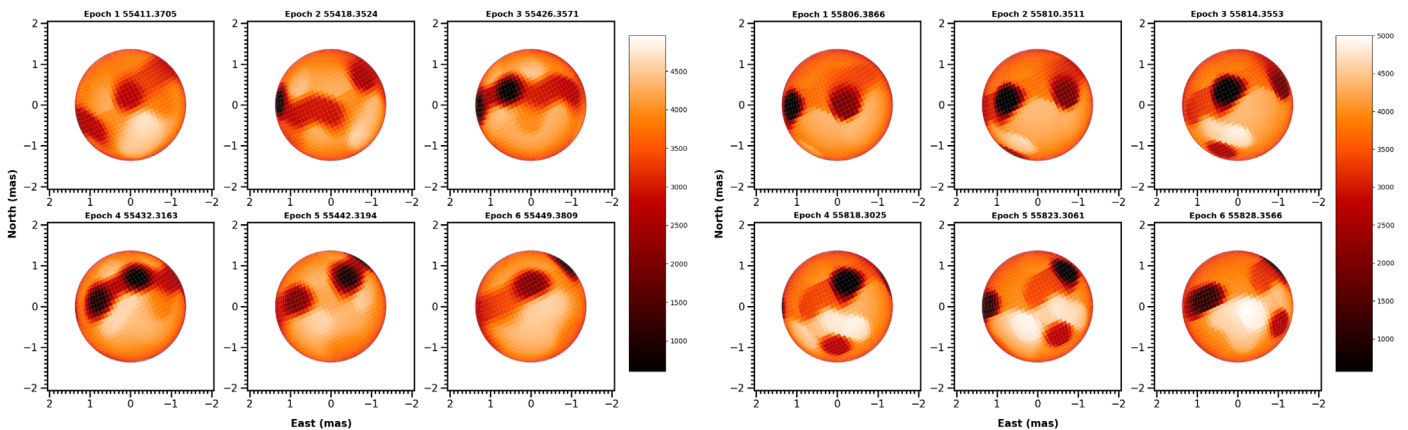


**Figure 7.** We show relative intensity maps (in arbitrary units) of  $\lambda$  Andromedae for the 2010 epoch (left) and 2011 epoch (right) using our ROTIR code. Here, we note that our 2010 intensity map panels do not reflect all 11 nights of data but only show a subset of 6 nights. The nights for the 2010 intensity map panels are chosen by only selecting one of two consecutive observational nights and having the next intensity map panel be separated by at least 6 nights (i.e., 2010 Aug 03, 2010 Aug 10, 2010 Aug 18, 2010 Aug 24, 2010 Sep 03, and 2010 Sep 10). All images here for both the 2010 and 2011 epochs reflect the same parameters that are listed in Table 4.

within NLOpt for these four parameters as follows: [1.35, 1.39] for angular radius, [0.2, 0.3] for the limb-darkening coefficient, [70.0, 90.0] for inclination, and [20.0, 30.0] for position angle. The final values for each variable parameter are chosen by averaging over all bootstraps and their associated errors are calculated through their standard deviation. Our 50 bootstraps do not show a Gaussian distribution, but we are prevented from running a large number of bootstraps due to computation time. We indicate that parameters do not deviate too largely from their mean values. It is likely that doing more bootstraps will slightly increase the error bars but not in a significant manner. We show the results of our bootstrap values in Figure 6.

### 5.3. Images of $\lambda$ And

Temperature maps are not indicative of what is actually represented from observations. In order to present an image, we include to use a power law for limb darkening (Hestroffer 1997) and multiply it by the cells of the temperature maps that are visible to the observer. We use the limb-darkening coefficient from our bootstrap to present the images in Figure 7 and present the physical parameters for the primary star in  $\lambda$  And using the parameters from our bootstrap in Table 4.

## 6. Comparisons to Previous Work

### 6.1. SURFING vs. ROTIR Imaging

Here, we compare images made independently from ROTIR to another image reconstruction code called SURFACE imaging (SURFING) in Figure 8. SURFING is a Monte Carlo-based imaging code written in IDL specifically written for imaging spheroids (see Roettenbacher et al. 2016b). Overall, there is a good agreement between the two imaging methods. Since we are only focusing on the imaging comparison aspect for these two codes, we see that the spot locations and contrast between the two are very similar, with a few minor differences, as shown in Figures 5 and 8.

### 6.2. Comparison to Parks et al.

The results of this work largely agree to those of Parks et al. (2021) with the exception of the inclination of  $\lambda$  And being the only disagreement. Parks et al. (2021) used a combination of a genetic algorithm (Charbonneau 1995) and the Nelder–Mead simplex method (Nelder & Mead 1965; Box 1965; Richardson & Kuester 1973), in order to make individual models for each night of data. Each surface model calculates an angular diameter, limb-darkening coefficient based on the power law,

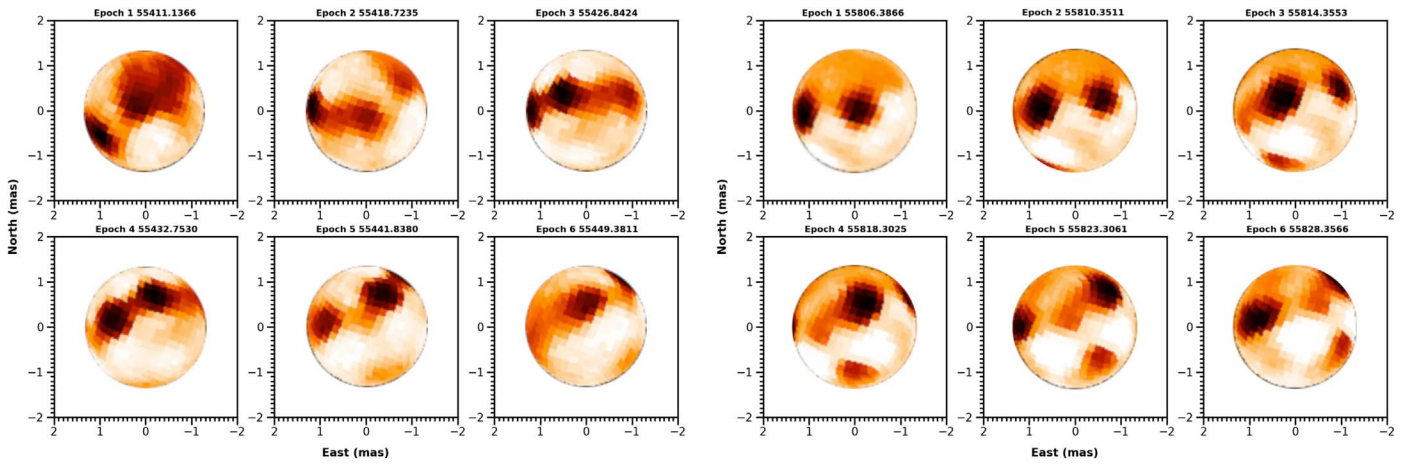


**Figure 8.** Temperature maps of  $\lambda$  Andromedae in 2010 (left) and 2011 (right) using SURFING code. The 2010 temperature maps (in similar Kelvin scale to Figure 5) were made by using two different consecutive nights and merging the data as one night. We find that this does not largely affect the results of the imaging since the rotation made from two consecutive nights only span  $\sim 2\%$  of the rotation period.

**Table 4**  
Final  $\lambda$  Andromedae Parameters for the Primary

Observed Parameters	Value	Source	Values from the Literature	Literature Reference
$R_*$ (mas)	$1.371 \pm 0.005$	This work	$1.379 \pm 0.025$	Parks et al. (2021)
Limb-darkening coefficient	$0.231 \pm 0.024$	This work	$0.229 \pm 0.111$	Parks et al. (2021)
Inclination (deg)	$85.63 \pm 2.32$	This work	$70.35 \pm 6.7^d$	Parks et al. (2021)
Position angle (deg)	$26.09 \pm 0.82$	This work	$21.6 \pm 7.5^d$	Parks et al. (2021)
Rotation period (days)	54.2	This work	$56.9 \pm 8.8^d$	Parks et al. (2021)
Physical parameters				
$R_*$ ( $R_\odot$ )	$7.787 \pm 0.053$	This work <sup>a</sup>	$7.831^{+0.067}_{-0.065}$	Parks et al. (2021)
$T_{\text{eff}}$ (K)	$4800 \pm 100$	Drake et al. (2011)	...	...
$\log g$	$2.75 \pm 0.25$	Drake et al. (2011)	...	...
$M_*$ ( $M_\odot$ )	$1.24 \pm 0.72$	This work <sup>b</sup>	$1.3^{+1.0}_{-0.7}$	Drake et al. (2011)
$\log L/L_\odot$	$1.46 \pm 0.04$	This work <sup>c</sup>	$1.37 \pm 0.04$	Drake et al. (2011)
Distance (pc)	$26.41 \pm 0.15$	van Leeuwen (2007)	...	...

**Notes.** The observed parameters were optimized through a bootstrap approach with the exception of the rotation period, which was fixed. We take our fixed rotation period parameter directly from the best model in SIMTOI.

<sup>a</sup> Based on the angular radius from this work and the distance from van Leeuwen (2007).

<sup>b</sup> Based on the physical radius from this work and the  $\log g$  from Drake et al. (2011).

<sup>c</sup> Based on the physical radius from this work and the effective temperature from Drake et al. (2011).

<sup>d</sup> Since Parks et al. (2021) had multiple values reported for the same parameter, we show the averages of the respective parameter here.

a starspot covering factor, starspot latitude, starspot longitude, and starspot intensity ratio for  $\lambda$  And. Once all the models were made, Parks et al. (2021) traced each starspot on the surface for each epoch. Ellipse fits to starspot positions were calculated, and an average computed position angle and inclination angle were made from these ellipse fits for each year.

Parks et al. (2021) reported that the inclination of primary from their 2010 and 2011 data is  $75 \pm 5.0^\circ$  and  $66.4^\circ \pm 8.0^\circ$ , for each respective year, giving an overall average of  $70.35^\circ \pm 6.7^\circ$  while we report an inclination of  $85.63^\circ \pm 2.32^\circ$ . We believe that our calculations from this work are accurate for several reasons. The initial SIMTOI calculations were done with a global search with no restrictions in parameter space, including inclination. The resulting parameters obtain from SIMTOI were then used in ROTIR with a sufficient range that included the inclination value from Parks et al. (2021). If the value for our inclination were incorrect and actually leaned toward this previous value, the

resulting bootstrap method would have reflected it by converging on the lower bounds of our parameter space using our bootstraps. In addition, the work by Parks et al. (2021) relied on independent models for each night and tied them together to form an analysis while we use all the data of each epoch collectively to form one image.

## 7. Beyond Solid Rotation Imaging

### 7.1. Simulating Differential Rotation

In our Figures 4–8 using SIMTOI/ROTIR, SURFING, and in Parks et al. (2021), all imaging has been performed assuming that the star is rotating as a solid body however, we attempt to estimate differential rotation through our data. Henry et al. (1995) studied photometry of  $\lambda$  And over 14 yr and found evidence of shear across the surface. In order to see if we are able to detect any differential rotation with our interferometric data, we simulate starspots on a star with a low differential

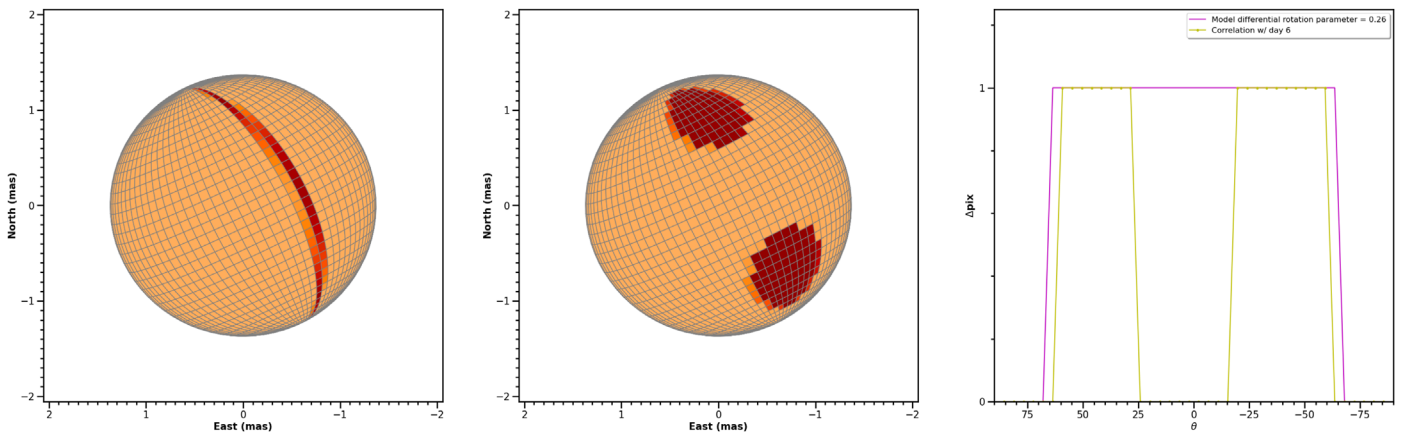


**Figure 9.** We show simulations of differential rotation by doing a correlation using the unrealistic starspot among a longitudinal band (left) and two starspots (middle) of a fake star with the same parameters of  $\lambda$  Andromedae within the 2011 epoch (with the exception of the temperature map). The differential rotation coefficient we use here is  $\Delta\Omega$  of 0.26 from Henry et al. (1995). The plot (right) shows the number of pixels that have shifted in respect to the longitude after subtracting off the total shift of a spot for a given latitude. The pink line at this coefficient represents the unrealistic starspot change in pixels while the yellow line shows the two starspots change in pixels as a function of the longitude. We choose to compare the first and last observations within the 2011 epoch to show the maximum amount of correlation.

rotation coefficient and a low temperature gradient on the surface, and have the spot move across a few days with the same period as  $\lambda$  And. Then we do a cross correlation for each latitude band on the star and see if there is any deviation from zero.

Our simulations show two different scenarios. The first simulation presents a highly unrealistic starspot is are two pixels wide in longitude and spanning throughout all latitude from pole to pole. Our second simulation shows two circular starspots that are 5 pixels in radius at  $+45^\circ$  and  $-45^\circ$  latitude (in respect to the equator) and at  $135^\circ$  longitude. We present our simulations of a simple star with similar parameters as  $\lambda$  And using differential rotation coefficient from Henry et al. (1995) of  $k=0.04$ , which corresponds to differential angular velocity ( $\Delta\Omega$ ) of 0.26, in Figure 9.

### 7.2. Testing Differential Rotation on $\lambda$ And

We apply the same cross-correlation method for the 2011 data set and calculate the deviations. We find that we are unable to detect any differential rotation with our data due to three reasons. First, our data does not span an entire rotation, therefore we are not able to compare the same spots from the previous rotation. Second,  $\lambda$  And is a very slow rotator so we do not have enough resolution to detect any small amounts of differential rotation, if differential rotation truly exists on  $\lambda$  And. In fact, the large scale magnetic spots on  $\lambda$  And may not be able to be used to measure any real surface differential rotation based on its dynamo. Korhonen & Elstner (2011) states that surface differential rotation can only be recovered by observing the spot motion of small spots, unlike  $\lambda$  And’s large scale magnetic spot structure. Third, the amount of square visibilities and closure phases for each observation are sparse for most observations. Since the goal is to detect any shear as evidence for differential rotation, we reconstruct an individual temperature map for each observation date from the 2011 epoch but initialize with the temperature map obtained from Figure 4. We show our results in Figure 10.

## 8. Beyond Imaging the Primary

### 8.1. Updated Orbital Parameters and Secondary Parameters

Using the updated parameters from the primary star in  $\lambda$  And in this work, the mass ratio from Donati et al. (1995) and Kepler’s Third Law, we are now able to calculate the mass of the secondary and the semimajor axis of the binary system. We calculate that the mass for the companion is  $0.15^{+0.09}_{-0.05} M_\odot$  and with corresponding semimajor axis is 6.12 mas for the system.

### 8.2. The Search for the Secondary

We begin our search for the companion by obtaining an estimate on the luminosity ratio and angular size of the secondary to narrow down our search. For the luminosity ratio, we used a mass–luminosity relation for each corresponding star in our system ( $L_2/L_1 = 0.23(M_2^{2.3}/M_1^4)$ ) and calculated to be approximately  $L_2/L_1 = 0.00121$ . If we assume that the  $H$ -band flux ratio is the same as the luminosity ratio of the two stars and if we use the  $H$ -band magnitude of the primary 1.40 mag (Ducati 2002), this would correspond to an estimated  $H$ -band magnitude of 8.7 mag for the secondary. This is slightly beyond MIRC’s magnitude limit and not likely to be detected, however we still investigate the possibility of detection. In order to calculate the estimated angular size of the secondary, we first calculate the physical size by using the mass–radius relation ( $R = 0.0753 + 0.7009M + 0.2356M^2$ ) developed by Maldonado et al. (2015) for low-mass stars. Given that the calculated physical radius is  $0.19 R_\odot$ , we find that the estimated angular radius is approximately 0.03 mas.

Now that we have an estimation of the angular size and flux ratio, we perform a grid search in R.A. and decl. over a 10 mas distance from the primary star for every night in the 2011 epoch. This approach is similar the methods used in Baron et al. (2012) and CANDID (Gallenne et al. 2015) with the difference that the primary is using the model visibilities obtained during image reconstruction. We model binary visibilities and vary both the brightness ratio and the angular radius for the secondary using NLOpt for each section of the grid. We restrict the parameter space for the angular radius to

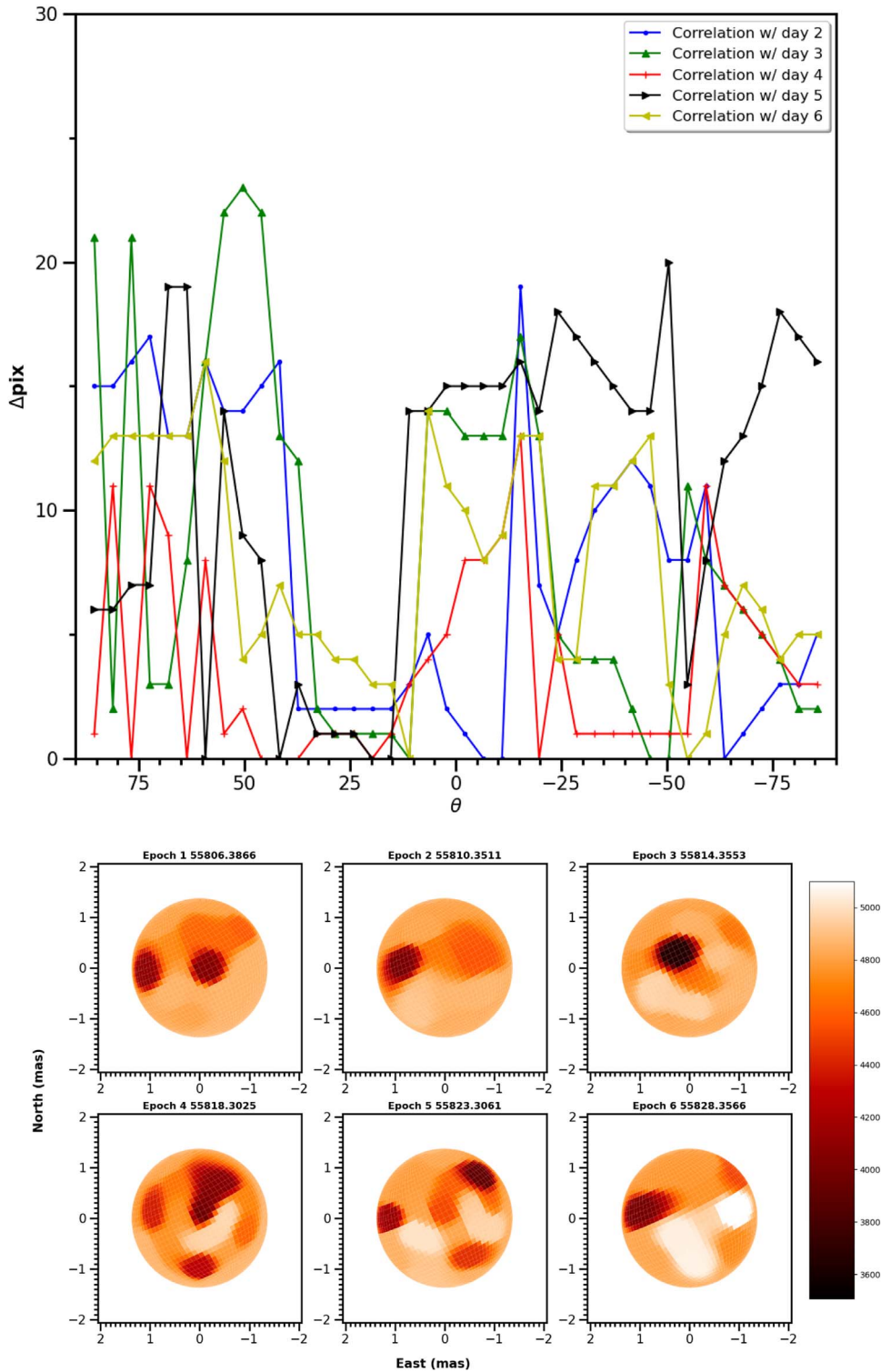


**Figure 10.** The plot shown here (top) is similar to that of Figure 9 but with the actual  $\lambda$  Andromedae data. The different symbols denote correlations of temperature maps compared to the first observation of  $\lambda$  Andromedae in the 2011 epoch. The individual temperature maps (in Kelvin) for each observation date in 2011 (bottom) were constructed using the original temperature map from Figure 4. These maps reflect the difficulty in searching for shear at the one pixel level since each map is slightly different compared to the previous observation and results in no visible correlation.

[0.0, 1.0] mas while restricting the flux ratio (secondary/primary flux) for the system from [0.0, 0.2].

While we do find that the average flux ratio using the 2011 data set of  $0.00213 \pm 0.00116$  is within the theoretical estimated value, we find two major reasons for believing that we were not able to find the secondary companion. First, the

average angular radius found by using the 2011 data is  $0.602 \pm 0.356$  mas, largely inconsistent with our estimation using mass–radius relation for low-mass stars. Our errors for both the flux ratio of the system and the angular size of the secondary were calculated by taking the standard deviation of every night’s grid search result from the 2011 epoch. The

values of angular radius for an individual night were also seen to hit a boundary condition (either 0 mas or 1 mas), thus assessing that the calculated values are incorrect. Second, the best fit R.A. and decl. positions for each night in the 2011 data set were positioned in a random assortment on the grid space with no clear indication of a circular or elliptical orbit.

Another reason that we may not be able to find the secondary for  $\lambda$  And could be due to lack of  $(u, v)$  coverage for each individual night in the 2011 epoch data set. For this reason, we proceed to not use the 2010 data set to find the secondary as those observations were taken with two different sets of 4T observations in a given night and as a result do not provide better  $(u, v)$  coverage compared to the 2011 data set.

## 9. Conclusion and Future Prospects

In this paper, we do interferometric modeling and imaging on  $\lambda$  And for the 2010 and 2011 epochs. First, we use SIMTOI in order to find which model is most probable for finding the best parameters. Then we use the parameters from SIMTOI and use them for imaging in ROTIR. Using the parameters from the best SIMTOI model as a starting point, we apply the bootstrap method to get the final physical parameters for  $\lambda$  And. We find that our images from ROTIR fairly agree with the images produced to the other image reconstruction code, SURFING, and our physical parameters are also fairly consistent of previous works with the exception of the inclination.

Images from both codes show that the spots on  $\lambda$  And from both epochs seem to favor certain latitudes and are mostly concentrated in the northern hemisphere. For both the 2010 and 2011 epochs, we find that most of the spots are centered around  $+20^\circ$  latitude. These spot concentrations to a certain latitude are consistent with the interferometric images shown in Roettenbacher et al. (2016b) of  $\zeta$  Andromedae, another RS CVn variable. The absence of symmetrical spots on active latitudes as observed on the Sun is evidence that  $\lambda$  And may not have a solar-like dynamo.

Finally, once we produce static images of the primary star in the system, we test to see if we find any evidence for differential rotation and detect the secondary companion. We start with a simulation of differential rotation and compare those results to the 2011 interferometric data set. Our results remain inconclusive as we cannot detect any shear within the 2011 data set largely due to  $\lambda$  And being a slow rotator. In our search for the companion, we do a grid search by fitting various models for the companion (i.e., varying the angular radius of the secondary and flux ratio of the system). While the flux ratio was consistent with the approximated value, the angular radius was largely inconsistent with our estimated calculation therefore concluding that we were unable to detect the secondary.

Our ROTIR code is not just limited to interferometric imaging but is also capable of light-curve inversion. Our future work will plan on using the multiband photometry in Parks et al. (2021) and compare those resulting images with the interferometric images from this work. Our plans also include using the photometric data as a bridge for the 2010 and 2011 interferometric epochs in order to detail how  $\lambda$  And is evolving over the course of a year. We have are currently implementing additional numerical techniques to ROTIR (Abbott et al. 2021) in order to improve light-curve inversion quality with the use of Alternating Direction Method of Multipliers (Chan et al. 2011).

Finally, we have future plans to implement Doppler imaging and Zeeman-Doppler imaging into ROTIR.





The authors thank the anonymous referee for the insightful comments that improved the quality of the manuscript. A.O.M. and F.R.B. acknowledge support from NSF grant No. AST-1616483 and AST-1814777. R.M.R. acknowledges support from the Yale Center for Astronomy and Astrophysics (YCAA) Prize Postdoctoral Fellowship.

This work is based upon observations obtained with the Georgia State University Center for High Angular Resolution Astronomy Array at Mount Wilson Observatory. The CHARA Array is supported by the National Science Foundation under grant No. AST-1636624 and AST-1715788. Institutional support has been provided from the GSU College of Arts and Sciences and the GSU Office of the Vice President for Research and Economic Development. Any opinions, findings, and conclusions or recommendations expressed in this material are those of the author(s) and do not necessarily reflect the views of the National Science Foundation.

*Facility:* The Center of High Angular Resolution Astronomy Array.

*Software:* SIMTOI, OITTOOLS, ROTIR.

## ORCID iDs

Arturo O. Martinez  <https://orcid.org/0000-0002-3311-4085>  
 Fabien R. Baron  <https://orcid.org/0000-0002-8376-8941>  
 John D. Monnier  <https://orcid.org/0000-0002-3380-3307>  
 Rachael M. Roettenbacher  <https://orcid.org/0000-0002-9288-3482>

## References

- Abbott, C. G., Baron, F., & Martinez, A. O. 2021, in press
- Baglin, A., Auvergne, M., Boisnard, L., et al. 2006b, in 36th COSPAR Scientific Assembly (Paris: ESA), 3749
- Baglin, A., Michel, E., Auvergne, M. & COROT Team 2006a, in ESA Special Publication, 624, Proc. of SOHO 18/GONG 2006/HELAS I, Beyond the Spherical Sun (Paris: ESA), 34
- Barnes, T. G., Evans, D. S., & Moffett, T. J. 1978, *MNRAS*, 183, 285
- Baron, F., & Martinez, A. O. 2018, Interferometric Imaging and Light Curve Inversion on Rotating Spheroids, <https://github.com/fabienbaron/ROTIR.jl>
- Baron, F., & Martinez, A. O. 2021, in press
- Baron, F., Monnier, J. D., Pedretti, E., et al. 2012, *ApJ*, 752, 20
- Baron, F., Norris, R. P., & Martinez, A. O. 2019, OITTOOLS: the All-in-One Tool Package for Optical Interferometry, <https://github.com/fabienbaron/OITTOOLS.jl>
- Bonneau, D., Clausse, J. M., Delfosse, X., et al. 2006, *A&A*, 456, 789
- Borucki, W. J., Koch, D., Basri, G., et al. 2010, *Sci*, 327, 977
- Box, M. J. 1965, *CompJ*, 8, 42
- Chane, S. H., Khoshabeh, R., Gibson, K. B., Gill, P. E., & Nguyen, T. Q. 2011, *ITIP*, 20, 3097
- Charbonneau, P. 1995, *ApJS*, 101, 309
- Che, X., Monnier, J. D., Tycner, C., et al. 2012, *ApJ*, 757, 29
- Che, X., Monnier, J. D., Zhao, M., et al. 2011, *ApJ*, 732, 68
- Chu, F.-L., & Huang, C.-F. 1989, *JPhA*, 22, L671
- Davenport, J. R. A., Hebb, L., & Hawley, S. L. 2015, *ApJ*, 806, 212
- Donati, J.-F., Henry, G. W., & Hall, D. S. 1995, *A&A*, 293, 107
- Drake, J. J., Ball, B., Eldridge, J. J., Ness, J.-U., & Stancliffe, R. J. 2011, *AJ*, 142, 144
- Ducati, J. R. 2002, VizieR Online Data Catalog: Catalogue of Stellar Photometry in Johnson's 11-color system
- Eker, Z., Ak, N. F., Bilir, S., et al. 2008, *MNRAS*, 389, 1722
- Feroz, F., & Hobson, M. P. 2008, *MNRAS*, 384, 449
- Feroz, F., Hobson, M. P., & Bridges, M. 2009, *MNRAS*, 398, 1601
- Feroz, F., Hobson, M. P., Cameron, E., & Pettitt, A. N. 2013, *OJAp*, 2, 10
- Frasca, A., Fröhlich, H. E., Bonanno, A., et al. 2011, *A&A*, 532, A81
- Fröhlich, H. E., Frasca, A., Catanzaro, G., et al. 2012, *A&A*, 543, A146

- Gallenne, A., Mérand, A., Kervella, P., et al. 2015, *A&A*, **579**, A68
- Goncharskii, A. V., Stepanov, V. V., Kokhlova, V. L., & Yagola, A. G. 1977, *SvAL*, **3**, 147
- Górski, K. M., Hivon, E., Banday, A. J., et al. 2005, *ApJ*, **622**, 759
- Hall, D. S. 1976, in *Astrophysics and Space Science Library*, The RS CVn Binaries and Binaries with Similar Properties, ed. W. S. Fitch, Vol. 60 (Dordrecht: D. Reidel Publishers), 287
- Harmon, R. O., & Crews, L. J. 2000, *AJ*, **120**, 3274
- Henry, G. W., Eaton, J. A., Hamer, J., & Hall, D. S. 1995, *ApJS*, **97**, 513
- Hestroffer, D. 1997, *A&A*, **327**, 199
- Johnson, S. G. 2008, The NLOpt nonlinear-optimization package, <https://github.com/stevengj/nlopt>
- Kóvári, Z., Kriskovics, L., Künstler, A., et al. 2015, *A&A*, **573**, A98
- Kloppenborg, B., & Baron, F. 2012a, *LibOI: The OpenCL Interferometry Library*, Version 1.0.0., <https://github.com/bkloppenborg/liboi>
- Kloppenborg, B., & Baron, F. 2012b, *SIMTOI: Simulation and Modeling Tool for Optical Interferometry*, Version 1.1.1., <https://github.com/bkloppenborg/simtoi>
- Kloppenborg, B., Stencel, R., Monnier, J. D., et al. 2010, *Natur*, **464**, 870
- Kloppenborg, B. K., Stencel, R. E., Monnier, J. D., et al. 2015, *ApJS*, **220**, 14
- Koch, D. G., Borucki, W. J., Basri, G., et al. 2010, *ApJL*, **713**, L79
- Korhonen, H., & Elstner, D. 2011, *A&A*, **532**, A106
- Lee, S.-W., & Mittra, R. 1983, *ITAP*, **31**, 99
- Maldonado, J., Affer, L., Micela, G., et al. 2015, *A&A*, **577**, A132
- McInturff, K., & Simon, P. S. 1991, *ITAP*, **39**, 1441
- Monnier, J. D., Berger, J.-P., Millan-Gabet, R., & ten Brummelaar, T. A. 2004, *Proc. SPIE*, **5491**, 1370
- Monnier, J. D., Che, X., Zhao, M., et al. 2012, *ApJL*, **761**, L3
- Monnier, J. D., Zhao, M., Pedretti, E., et al. 2007, *Sci*, **317**, 342
- Mourard, D., Monnier, J. D., Meilland, A., et al. 2015, *A&A*, **577**, A51
- Nelder, J., & Mead, R. 1965, *Comput.J.*, **7**, 308
- Nielsen, M. B., Gizon, L., Cameron, R. H., & Miesch, M. 2019, *A&A*, **622**, A85
- Parks, J. R., White, R. J., Baron, F., et al. 2021, *ApJ*, **913**, 54
- Piskunov, N. E., & Wehlau, W. H. 1990, *A&A*, **233**, 497
- Renard, S., Thiébaud, E., & Malbet, F. 2011, *A&A*, **533**, A64
- Rice, J., Wehlau, W., Khokhlova, V. L., & Piskunov, N. E. 1981, in *Liege Int. Astrophysical Colloquia*, 23, *Liege Int. Astrophysical Colloquia*, 265
- Richardson, J. A., & Kuester, J. L. 1973, *Commun. ACM*, **16**, 487
- Roettenbacher, R. M., Kane, S. R., Monnier, J. D., & Harmon, R. O. 2016a, *ApJ*, **832**, 207
- Roettenbacher, R. M., Monnier, J. D., Harmon, R. O., Barclay, T., & Still, M. 2013, *ApJ*, **767**, 60
- Roettenbacher, R. M., Monnier, J. D., Korhonen, H., et al. 2016b, *Natur*, **533**, 217
- Roettenbacher, R. M., Monnier, J. D., Korhonen, H., et al. 2017, *ApJ*, **849**, 120
- Santos, A. R. G., García, R. A., Mathur, S., et al. 2019, *ApJS*, **244**, 21
- Schaefer, G. H., Brummelaar, T. T., Gies, D. R., et al. 2014, *Natur*, **515**, 234
- Somers, G., & Pinsonneault, M. H. 2015, *ApJ*, **807**, 174
- Strassmeier, K. G. 2009, *A&ARv*, **17**, 251
- ten Brummelaar, T. A., McAlister, H. A., Ridgway, S. T., et al. 2005, *ApJ*, **628**, 453
- Thiebaud, E. 2002, *Proc. SPIE*, **4847**, 174
- van Leeuwen, F. 2007, *A&A*, **474**, 653
- von Zeipel, H. 1924, *MNRAS*, **84**, 665
- Walker, E. C. 1944, *JRASC*, **38**, 249
- Wild, W. J. 1989, *PASP*, **101**, 844
- Zhao, M., Gies, D., Monnier, J. D., et al. 2008, *ApJL*, **684**, L95
- Zhao, M., Monnier, J. D., Che, X., et al. 2011, *PASP*, **123**, 964
- Zhao, M., Monnier, J. D., Pedretti, E., et al. 2009, *ApJ*, **701**, 209